

Learning Discontinuous Piecewise Affine Fitting Functions using Mixed Integer Programming for Segmentation and Denoising

Ruobing Shen · Bo Tang · Leo Liberti ·
Claudia D'Ambrosio · Stéphane Canu

Received: date / Accepted: date

Abstract Piecewise affine functions are widely used to approximate nonlinear and discontinuous functions. However, most, if not all existing models only deal with fitting continuous functions. In this paper, We investigate the problem of fitting a discontinuous piecewise affine function to given data that lie in an orthogonal grid, where no restriction on the partition is enforced (i.e., its geometric shape can be nonconvex). This is useful for segmentation and denoising when data correspond to images. We propose a novel Mixed Integer Program (MIP) formulation for the piecewise affine fitting problem, where binary variables determines the location of break-points. To obtain consistent partitions (i.e. image segmentation), we include multi-cut constraints in the formulation. Since the resulting problem is \mathcal{NP} -hard, two techniques are introduced to improve the computation. One is to add facet-defining inequalities to the formulation and the other to provide initial integer solutions using a special heuristic algorithm. We conduct extensive experiments by some synthetic images as well as real depth images, and the results demonstrate the feasibility of our model.

Keywords Piecewise affine fitting · Mixed integer programming · Cutting plane · Facet-defining inequalities · Image processing .

Ruobing Shen
Institute of Computer Science, Universität Heidelberg, 69120 Heidelberg, Germany
E-mail: ruobing.shen@informatik.uni-heidelberg.de

Bo Tang
College of Science, Northeastern University, Boston 02115, USA

Leo Liberti, Claudia D'Ambrosio
LIX CNRS, École Polytechnique, Institut Polytechnique de Paris, 91128 Palaiseau, France

Stéphane Canu
INSA de Rouen, Normandie Université, 76801 Saint Etienne du Rouvray, France

1 Introduction

Let $D \subseteq \mathbb{R}^d$ denote the signal domain, and $y : D \rightarrow \mathbb{R}$ denote intensity values of the given signals, possibly with some noise. In this paper, we seek to find (or approximate) a discontinuous piecewise affine function that best fits the data y over D , where D is restricted to an orthogonal grid. Although it can be generalized to higher dimensions, we are mostly interested in the scenario when $d = 2$, where D is a square grid and y corresponds to natural or depth images.

In statistics, *affine (linear) regression* or *affine fitting* is a widely used approach to model the relationship between the data y and the independent variables $z \in D$, which are, in our case, the coordinates of y . In the parametric model, the relationship is modeled using affine functions. The unknown affine parameters β (i.e., slopes and intercepts) are estimated from the given data according to some standard objective functions, such as the well-known mean square error (MSE) [19].

Non-parametric models, on the other hand, assume that the data distribution cannot be defined in terms of such a finite set of parameters β . Typically, the model grows in size according to the complexity of the data. For instance, one can introduce some fitting variables w to model the data y ; some assumptions are then made about the connections among these variables.

We call a function f (*possibly discontinuous*) *piecewise affine* over D if there is a partition of D into disjoint subsets D_1, \dots, D_k such that f is affine when restricted to each D_i (we denote by f^i the function f restricted to D_i). Let \mathcal{D} be the set of all partitions of D , and \mathcal{F} be the set of all piecewise affine functions over D , then any choice of $f \in \mathcal{F}$ defines $\mathcal{D}' \in \mathcal{D}$. Moreover, if the partition \mathcal{D}' is known, the corresponding $f \in \mathcal{F}$ can be easily identified by computing the affine parameters β within each region D_i under some objectives (e.g. MSE).

The problem of piecewise affine fitting has been studied for decades. Numerous clustering based algorithms [24,4,5] are designed for different variants of the problem, but only suffice to find local optimal solutions. Exact formulations of the problem via MIP are also proposed, but often with restrictions. Examples include the continuous piecewise linear fitting models [23], where the domain partition is in a sense pre-defined, and the fitting function f is restricted to be continuous over D . A general n -dimensional piecewise linear fitting problem has been studied in [1], and formulated as a parametric model using MIP. But the assumption that the segments are linearly separable does not hold in many practical applications.

In this paper, we will focus on the non-parametric model that finds (or approximates) a possibly discontinuous piecewise affine function $f \in \mathcal{F}$ to fit the data y , where the affine regions are unknown and the affine parameters within each D^i are not explicitly computed. Our problem can be mathematically represented as follows:

$$\min_{\mathcal{D}' \in \mathcal{D}, w} \sum_{D_i \in \mathcal{D}'} \left(\int_{D_i} |(f^i(z) - y(z))| dz + \lambda Per(D_i) \right) \quad (1)$$

$$f(z) = w(z), \quad (1a)$$

where $Per(D_i)$ denotes the perimeter of D_i and λ is a regularization parameter. The first term measures the quality of data fitting, and the second regularization

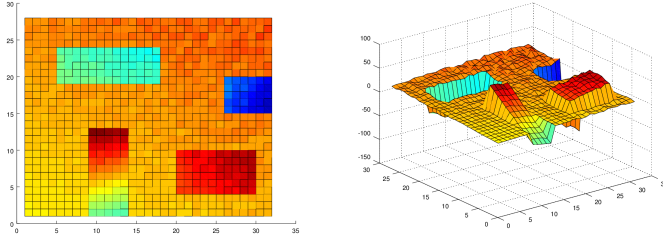


Fig. 1: A synthetic 2D image with noise that has linear trend and its 3D view.

term is used to balance the former with the number and the boundary length of segments (affine regions), to prevent over-fitting. Note that an absolute fitting term is adopted here to enable a Mixed Integer Linear Programming (MILP) formulation of the model. Being a non-parametric model, further constraints on the fitting variables w will be defined to model the linearity within D_i , in Section 2 and 3.

Figure 1 shows a synthetic image with noise that has linear trends and its 3D view, where the horizontal axes (z_1 and z_2) represent the coordinates of the image pixels. Upon finding a piecewise affine function f , we also have a segmentation (to be introduced in next section) of the image into background and four segments, and a denoised image (with fitted value w) as a by-product.

1.1 Related work

For denoising (fitting) 2D images, the total variation (TV) model [17] is widely used

$$\min_w \int_D (w(z) - y(z))^2 dz + \lambda \text{TV}(w), \quad (2)$$

where the first part is the squared data fitting term (w the fitting function) and the second part is the regularization term. The TV regularizers can be either isotropic or anisotropic. The latter can be mathematically described as follows:

$$\text{TV}_{ani}(w) = \int_D (|\partial_{z_1} w| + |\partial_{z_2} w|) dz,$$

where ∂_{z_i} represents the partial derivative of w with respect to z_i , for $i = 1, 2$. Lysaker and Tai [14] provide a second-order regularizer

$$R_2(w) = \int_D (|\partial_{z_1 z_1} w| + |\partial_{z_2 z_2} w|) dz,$$

which better fits the scenarios of this paper.

Let $[n]$ denote the discrete set $\{1, 2, \dots, n\}$. Given n signals with coordinates $[n]$ and the n dimensional data vector \mathbf{y} , the classical (discrete) piecewise constant Potts model [16] has the form

$$\min_{\mathbf{w}} \|\mathbf{w} - \mathbf{y}\|_2 + \lambda \|\nabla^1 \mathbf{w}\|_0, \quad (3)$$

where $\|\cdot\|_2$ denotes the ℓ_2 norm, and $\|\cdot\|_0$ the ℓ_0 norm. The *discrete first derivative* $\nabla^1 \mathbf{w}$ of the fitting vector $\mathbf{w} \in \mathbb{R}^n$ is the $n - 1$ dimensional vector $(w_2 - w_1, w_3 - w_2, \dots, w_n - w_{n-1})$ and the ℓ_0 norm of a vector is its number of nonzero entries. The case of 2D images can be easily generalized.

Compared to the TV regularization term which over-penalizes the sharp discontinuities between two regions in an image, the ℓ_0 term in the Potts model is more desirable, but also computationally costlier. The discrete Potts model is in general \mathcal{NP} -hard to solve. The work of [7] was one of the first to utilize the Potts, and recently [21, 5] formulate it as a MIP that could find global optimum.

Apart from denoising, we also look into the segmentation problem. In graph based models, one first builds a square grid graph $G(V, E)$ to represent an image, where V corresponds to pixels of an image grid and E represents the 4 or 8 neighboring relations between pixels.

A graph partitioning \mathcal{V} is a partition of V into disjoint node sets $\{V_1, V_2, \dots, V_k\}$. And in graph-theoretical terms, the problem of image segmentation corresponds to graph partitioning. The *multicut* induced by \mathcal{V} is the edge set $\delta(V_1, V_2, \dots, V_k) = \{uv \in E \mid \exists i \neq j \text{ with } u \in V_i \text{ and } v \in V_j\}$. Hence, an image segmentation problem can be represented either by *node labeling*, i.e., assigning a label to each node $v \in V$, or by *edge labeling*, i.e., a multicut defined by a subset of edges $E' \subseteq E$, see the left image of Figure 5 as an example, where the multicut of 8 dashed edges uniquely defines a partition of the 4×4 -grid graph into 3 segments.

In machine learning, one often distinguishes between *supervised* and *unsupervised* segmentation. In the former case, the labels of classes (e.g., person, grass, sky, etc) are pre-defined, and annotated data is needed to train the model. Among many existing supervised models, the classical Markov Random Field (MRF) is well studied, and interested readers may refer to [22] for an overview of this field. Recently, Deep Convolutional Neural Networks [13] (DCNN) have become increasingly important in many computer vision tasks, such as semantics and instance segmentation [20, 8]. However, huge amount of annotation effort (in terms of pixel level annotated data) and computational budget (in terms of number of GPUs and training time) are needed.

In the unsupervised case, the labels' class information is missing. This introduces ambiguities when node labeling is used. See for example the node labeling in Figure 5. If we permute the labels (colors), it will result in the same segmentation. On the contrary, edge labeling (e.g., by multicuts) does not exhibit such symmetries and is therefore more appealing in this case. Recent notable approaches are the (lifted) multicut problems [10, 9, 11] based on Integer Linear Programming (ILP) formulations, which label edges (0 or 1) instead of pixels. The *multicut constraints* [11] (introduced in Section 3.2) are used to enforce a valid segmentation. These methods do not require annotated data and can be run directly on CPUs. In this paper, we will focus on this approach.

In this work, we borrow ideas from the second derivative TV and Potts model, and propose a novel MILP formulation for the discontinuous piecewise affine fitting problem. The original contributions of this paper are as follows.

- We propose an approximate and non-parametric model for the general discontinuous piecewise affine fitting problem.

- The model is formulated as a MILP and multicut constraints are added using cutting plane method to ensure a valid segmentation.
- The piecewise affine function can be easily constructed given the segmentation.

2 MIP for the piecewise linear fitting model: 1D

We first restrict ourselves to the simple 1D signals case where the signal domain $D \subseteq \mathbb{Z}^1$ (could be easily generalized to $D \subseteq \mathbb{R}^1$). Our model is able to find the optimal piecewise linear function $f \in \mathcal{F}$ that best fits the original data y .

2.1 Modeling as a MIP

The 1D signals with n discrete points could be naturally modeled as a chain graph. The associated graph $G(V, E)$ is defined with $V = \{i \mid i \in [n]\}$ and $E = \{e_i = (i, i + 1) \mid i \in [n - 1]\}$. We introduce $n - 1$ binary variables:

$$x_e = \begin{cases} 1, & \text{if two end nodes of edge } e \text{ are in different affine segments,} \\ 0, & \text{otherwise,} \end{cases}$$

where an edge e is called *active* if $x_e = 1$, otherwise it is *dormant*.

Our goal is to fit a piecewise linear function $f \in \mathcal{F}$ to the input data y . We denote the fitting value $w_i := f(z_i)$, for $i \in [n]$. The coordinate $z_i = i$ and denote x_{e_i} as x_i . We further define the following property:

$$\nabla^2 w_i = 0 \Leftrightarrow x_{i-1} = x_i = 0, \quad i \in [2 : n - 1], \quad (4)$$

where $\nabla^2 w_i := w_{i-1} - 2w_i + w_{i+1}$ is the discrete second derivative, and $[2 : n - 1]$ denotes the discrete set $\{2, 3, \dots, n - 1\}$.

The above property can be modeled via MIP using the “big M ” technique, which leads to the formulation

$$\min \sum_{i=1}^n |w_i - y_i| + \lambda \sum_{i=1}^{n-1} x_i \quad (5)$$

$$|\nabla^2 w_i| \leq M(x_{i-1} + x_i), \quad i \in [2 : n - 1], \quad (5a)$$

$$w_i \in \mathbb{R}, \quad i \in [n], \quad (5b)$$

$$x_i \in \{0, 1\}, \quad i \in [n - 1], \quad (5c)$$

where $\lambda > 0$ is similar to the regularization term in the Potts model (3). It is worth to mention that there are common tricks to formulate (5)-(5c) as a MILP. Namely, $|w| \leq Mx$ is replaced by two constraints $w \leq Mx$ and $-w \leq Mx$, and the absolute term $|w - y|$ in the objective function is replaced by $\epsilon^+ + \epsilon^-$, plus an additional constraint $w - y = \epsilon^+ - \epsilon^-$, where $\epsilon^+ \geq 0, \epsilon^- \geq 0$.

Lemma 1 *The optimal solution x^* of problem (5)-(5c) satisfies property (4).*

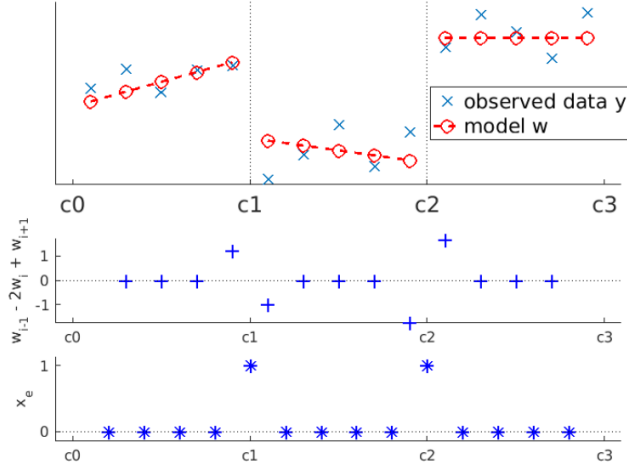


Fig. 2: An example with 3 affine segments and 2 active edges.

Proof The direction that $x_{i-1}^* = x_i^* = 0 \Rightarrow \nabla^2 w_i = 0$ directly follows constraint (5a). On the other hand, if $\nabla^2 w_i = 0$, the optimal solutions satisfy $x_{i-1}^* + x_i^* = 0$ (thus $x_{i-1}^* = x_i^* = 0$) since (5)-(5c) is a minimization problem with positive weights on x .

Figure 2 shows an example of 3 affine segments and 2 active edges computed by formulation (5)-(5c). We see that the optimal solution w_i is the fitting value for node i , and $x_i = 1$ acts as the boundary between two affine segments. As a result, the nodes between two active edges define one segment, and the signals within one segment share the same linear slope. Although being non-parametric, the linear parameters for each segment can be easily computed afterwards, and the number of segments equals $\sum_{i=1}^{n-1} x_i + 1$. Hence, upon solving the MIP formulation (5)-(5c) in $1D$, a piecewise linear function $f \in \mathcal{F}$ can be easily constructed, and $w_i := f(z_i), \forall i \in [n]$.

Note in the above example, the cases where $\nabla^2 w_i \neq 0$ actually induces $x_{i-1} + x_i = 1$, for some $i \in [2, n-1]$. However, there exists instances where $x_{i-1} + x_i = 2$ for $\nabla^2 w_i \neq 0$. The image on the left of Figure 3 depicts an example where the node 5 is an outlier (as an one node segment), and $x_{e_l} + x_{e_r} = 2$. We also observe that problem (5)-(5c) does not necessarily output unique optimal integer solution x . One extreme example is shown in the right image of Figure 3, where either x_{e_l} or x_{e_r} can be active (but not both), and they yield the same optimal objective value.

3 MIP of the piecewise affine fitting model: 2D

We are more interested in the 2D image case where the domain $D \subseteq \mathbb{Z}^2$. Our model is able to find the fitting value w and a valid segmentation. The optimal piecewise affine function can be approximated and constructed based on the segmentation.

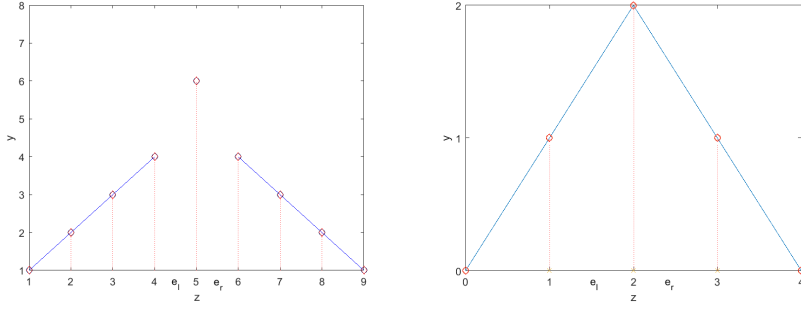


Fig. 3: Left: example where outlier exists (both e_l and e_r are active). Right: example with two segments where the optimal solution is not unique (either e_l or e_r is active).

3.1 Modeling as a MIP

A 2D image with $m \times n$ pixels could be naturally modeled as a square grid graph $G(V, E)$, where $V = \{(i, j) \mid i \in [m], j \in [n]\}$, and E represent the relations between the center and its 4 neighboring pixels (see Figure 5 for demonstration). Let $z_{i,j} = (i, j) \in \mathbb{Z}^2 \subseteq D$ be the coordinates for pixel (i, j) , and the matrix $Y = (y_{i,j}) \in \mathbb{R}^{m \times n}$ be the intensity values of the image. We divide the edge set E of the grid graph into its horizontal (row) edge set E^r and its vertical (column) edge set E^c . So $E = E^r \cup E^c$, and $E^r \cap E^c = \emptyset$. Denote $e_{i,j}^r \in E^r$ to present edge $((i, j), (i, j + 1))$ and $e_{i,j}^c \in E^c$ to represent $((i, j), (i + 1, j))$. Again for simplicity, we denote the binary edge variables $x_{e_{i,j}^r}^r := x_{e_{i,j}^r}$ and $x_{e_{i,j}^c}^c := x_{e_{i,j}^c}$.

The piecewise affine fitting model in 2D is obtained by formulating (5)-(5c) per row and column

$$\min \sum_{i=1}^m \sum_{j=1}^n |w_{i,j} - y_{i,j}| + \lambda \sum_{e \in E} x_e \quad (6)$$

$$|\nabla_r^2 w_{i,j}| \leq M(x_{i,j-1}^r + x_{i,j}^r), \quad i \in [m], j \in [2 : n-1], \quad (6a)$$

$$|\nabla_c^2 w_{i,j}| \leq M(x_{i-1,j}^c + x_{i,j}^c), \quad j \in [n], i \in [2 : m-1], \quad (6b)$$

$$w_{i,j} \in \mathbb{R}, \quad i \in [m], j \in [n], \quad (6c)$$

$$x_e \in \{0, 1\}, \quad e \in E, \quad (6d)$$

where M is again the big-M constant. Here, $\nabla_r^2 w_{i,j} = w_{i,j-1} - 2w_{i,j} + w_{i,j+1}$, and $\nabla_c^2 w_{i,j} = w_{i-1,j} - 2w_{i,j} + w_{i+1,j}$. That is, the discrete second derivative with respect to z_1 and z_2 -axis. Upon solving (6)-(6d), it serves for the purpose of denoising by computing w . But two questions still remain: does the binary solution x represent a valid segmentation? If so, is the corresponding piecewise affine function $f \in \mathcal{F}$ (obtained by affine fitting each segment) aligned with w , i.e., is $w_{i,j} = f(z_{i,j})$?

The answers to both questions are “no”, unfortunately. We will show in the next two sections that, the first one could be fixed by enforcing the multicut constraints. But the second one is not guaranteed, thus making our model approximate.

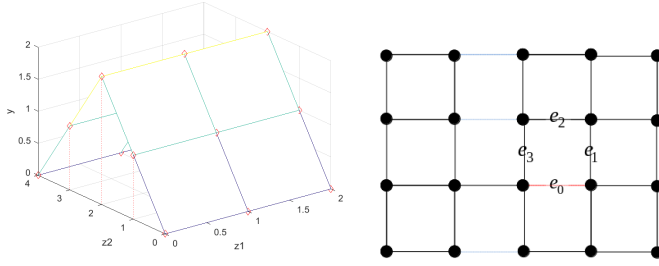


Fig. 4: A counter-example where model (6)-(6d) does not form a valid segmentation. Left: 3D view of input image. Right: the corresponding graph and active edges.

3.2 Multicut constraints for valid segmentation

The multicut constraints introduced in [2] are inequalities that enforce valid segmentation in terms of edge variables. It reads

$$\sum_{e \in C \setminus \{e'\}} x_e \geq x_{e'}, \quad \forall \text{ cycles } C \subseteq E, e' \in C, \quad (7)$$

which basically says that for any cycle, the number of active edges cannot be 1. Recall that an edge is called active if its two end nodes belong to different segments. Because otherwise, the two nodes of the active edge are again “linked” (hence belong to the same segment) by connecting the rest edges of the cycle, hence a contradiction.

We now prove the following lemma.

Lemma 2 *The multicut constraints (7) are needed for the optimal solution x of (6)-(6d) to form a valid segmentation.*

Proof We prove this lemma by constructing a counter-example as follows:

In the left image of Figure 4, the data terms y of all 15 pixels are constructed to lie exactly in two affine planes with respect to their coordinates $z = (z_1, z_2)$. The optimal affine function of the left plane is $y = 4 - z_2$ and the right one is $y = z_2$. We shall see that the 3 pixels with data $y = 2$ lie on both affine planes with respect to the coordinates z .

If we project the 3D plot into the z_2, y -space, for every row of the image grid, it is exactly the same 1D case we studied in the right image of Figure 3. We have showed there that the optimal solution is not unique.

Hence, we can easily construct one optimal solution x^* (3 blue edges plus 1 red edge) of (6)-(6d) shown in the right image of Figure 4, where the multicut constraints (7) is not satisfied. That is, there exists a cycle e_0 - e_1 - e_2 - e_3 that violates it.

3.3 The main formulation in 2D

We thus need to add the multicut constraints (7) to the piecewise affine fitting model (6)-(6d), to form a valid segmentation. This leads to the main formulation of our paper

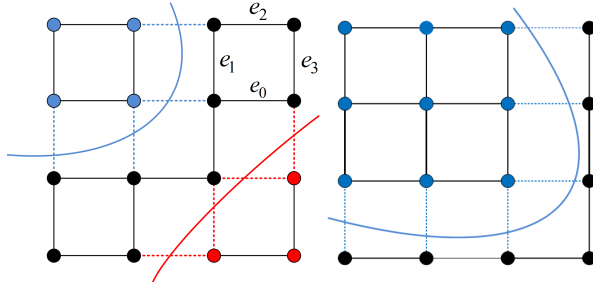


Fig. 5: Left: two representations of an image segmentation: node labeling (by colors) and edge labeling via multicuts (dashed edges). Right: example of a 9-pixel segment.

$$\min (1 - \lambda) \sum_{i=1}^m \sum_{j=1}^n |w_{i,j} - y_{i,j}| + \lambda \sum_{e \in E} x_e \quad (8)$$

$$|\nabla_r^2 w_{i,j}| \leq M(x_{i,j-1}^r + x_{ij}^r), \quad i \in [m], j \in [2 : n-1], \quad (8a)$$

$$|\nabla_c^2 w_{i,j}| \leq M(x_{i-1,j}^c + x_{ij}^c), \quad j \in [n], i \in [2 : m-1], \quad (8b)$$

$$\sum_{e \in C \setminus \{e'\}} x_e \geq x_{e'}, \quad \forall \text{ cycles } C \subseteq E, e' \in C, \quad (8c)$$

$$w_{ij} \in \mathbb{R}, \quad i \in [m], j \in [n], \quad (8d)$$

$$x_e \in \{0, 1\}, \quad e \in E. \quad (8e)$$

Note that the number of inequalities (8c) is exponentially large [2] with respect to $|E|$, where $|E|$ denotes the number of edges in G . Hence, in practice, it is not possible to include them into (8)-(8e) at one time. We will discuss in details in Section 4.2 the cutting plane algorithm that handles (8c).

It is well known that if a cycle $C \in G$ is chordless, then the corresponding multicut constraint (7) is facet-defining for the corresponding multicut polytope [10, 12]. Among all, the simplest ones of a grid graph are the 4 and 8-edge chordless cycle constraints (see the 4-edge cycle $e_0 - e_1 - e_2 - e_3$ in Figure 5 for an example), and the number of these constraints are linear to $|E|$. In Section 5, we will test different strategies of adding the 4 and 8-edge chordless cycle constraints to (8)-(8e) as initial constraints.

3.4 Approximate model for piecewise affine fitting

Finally, we prove the following theorem.

Theorem 1 *The MIP formulation (8)-(8e) is only approximate in finding the optimal piecewise affine fitting function $f \in \mathcal{F}$ that best fits y , i.e., (1a) does not hold.*

Proof We prove this theorem by constructing a counter-example where the optimal solution w^* of (8)-(8e) within one segment does not lie in any affine function f^i with respect to the coordinates z .

We construct an optimal solution x^* which corresponds to the segmentation in the right image of Figure 5, where the 9 nodes on the top left corner form a segment. We restrict ourselves to this segment where the integer coordinates of the pixels range from $(0, 0)$ to $(2, 2)$.

By constraint (8a), the w^* of the 3 nodes on each row satisfy the same linear function. Assume the linear function in the first and second row of nodes satisfy $w = a_1z + b_1$ and $w = a_2z + b_2$, where (a, b) are the linear parameters and z the discrete coordinates that range from 0 to 2 in this case. Then the fitting value w^* of the 6 nodes on the first two rows are listed in the following matrix:

$$\begin{bmatrix} w_{00} & w_{01} & w_{02} \\ w_{10} & w_{11} & w_{12} \end{bmatrix} = \begin{bmatrix} b_1 & a_1 + b_1 & 2a_1 + b_1 \\ b_2 & a_2 + b_2 & 2a_2 + b_2 \end{bmatrix}.$$

We can then compute w_{22} using constraint (8b), where $w_{22} = 2w_{12} - w_{02} = 4a_2 + 2b_2 - 2a_1 - b_1$. We note that if w^* of the 9 nodes lies in any affine function f^i , then $w_{00} - 2w_{11} + w_{22} = 0$.

However, we have $w_{00} - 2w_{11} + w_{22} = 2(a_2 - a_1)$, which is a contradiction when $a_1 \neq a_2$. Thus we complete the proof.

Although the MILP formulation (8)-(8e) is not exact on solving (1), we still get a valid segmentation. We can then fit an affine function within each segment afterwards, thus obtaining a valid (although not optimal) piecewise affine function $f \in \mathcal{F}$ as post-processing.

4 Solution Techniques

We now introduce a heuristic and an exact algorithms to solve (8)-(8e).

4.1 Region fusion based heuristic algorithm

The resulting problem (8)-(8e) is a MILP, which is solved using any off-the-shelf commercial MIP solvers. The underlying sophisticated algorithms are based on the branch and cut algorithm, where a good global upper bound usually helps to improve the performance. In the following, we will introduce a fast heuristic algorithm that provides a valid segmentation. It was then given to (8)-(8e) and upon solving a linear program, its solution is served as a global upper bound.

Our heuristic is based on the region fusion algorithm [15] which approximates the Potts model (3). We start by performing parametric affine fitting over the 4 groups (2×2 squared nodes) of each node, as shown in Figure 6. We take the group that has the minimum fitting MSE, and assign the affine parameters (a vector of 3 in 2D case) to that node. Note that nodes located on the borders of the grid graph only have 2 such groups, while corner nodes only have 1 group. Our algorithm then starts

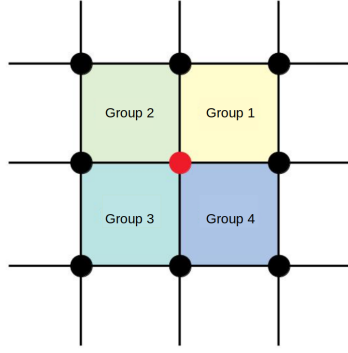


Fig. 6: Each node (colored red) has 4 groups of 2×2 squared nodes for affine fitting.

with every node i belonging to its own segment V_i , and for each pair of nodes, the following minimization problem is solved.

$$\min_{\mathbf{w}} \tau_i \|w_i - Y_i\|_2 + \tau_j \|w_j - Y_j\|_2 + \kappa_t \gamma_{ij} \mathbb{1}(w_i \neq w_j), \quad (9)$$

where $\mathbb{1}(\cdot)$ denotes the indicator function, τ_i the number of nodes in segment $V_i \subseteq V$, and γ_{ij} represents the number of neighboring nodes between two segments V_i and V_j . Here, Y_i indicates the affine parameter of segment V_i , and w_i the unknown variables, and κ_t express the regularization parameter at the k_{th} round of iteration.

To speed up computation, instead of solving (9) exactly, the following criteria is checked instead (see [15] for more detailed description):

$$\tau_i \tau_j \|Y_i - Y_j\|_2 \leq \kappa \gamma_{i,j} (\tau_i + \tau_j).$$

If the above condition holds, we merge segment V_i and V_j , and the updated affine parameter (also the values of w_i and w_j) is obtained by conducting a parametric affine fitting over the new segment. If not, the two segments and their affine parameters stay the same.

The algorithm iterates over each pair of nodes for solving (9), and the regularization parameter κ grows over every round of iteration, which increasingly encourages merging. The algorithm stops after t round of iteration, when $\kappa_t = \lambda$, where λ is the pre-defined regularization parameter with respect to (3).

4.2 Exact branch and cut algorithm

Apart from the classical branch-and-cut algorithm inside the MIP solver, we describes below the cutting plane method that iteratively add lazy constraints from (8c).

Cutting plane method. Similar to the cutting planes method that solves the multicut problem [10], we start solving (8)-(8e) by ignoring constraints (8c), or with few of them (e.g., the 4 or 8-edge cycle constraints).

We then check the feasibility of the resulting solution with respect to (8c). If it is already feasible, we are done and the optimal solution to (8)-(8e) is achieved. Otherwise, we identify the current separation problem and then add the corresponding violated constraints (cuts) to (8)-(8e). We resolve the updated MILP, and this procedure repeats until either we get the optimal solution, or the user-defined limit is reached.

Separation problem. Given an integer solution, it is polynomial to either check the feasibility with respect to (8c), or to identify and separate the integer infeasible solutions by adding violated constraints.

Phase 1: Given the incumbent solution of the MILP (8)-(8e), we extract its binary solutions and remove edges where $x_e = 1$ from the grid graph $G(V, E)$. We thus obtain a new graph $G'(V', E')$ where $V' = V$, $E' \subseteq E$ and we identify its connected components. We then check for each active edge to see if their two end nodes belong to the same component. If there exists any, the current solution is infeasible (and we call the corresponding active edges violated). Otherwise, a feasible and optimal solution is found.

Phase 2: If violated edges exist, we search for violated constraints by finding paths between the two nodes of the edge. We first conduct a depth-first search on the graph G' , and multiple such paths could be found. We set the maximum depth to 10 to restrict the searching time. If the depth-first search does not return any path, we then switch to the breadth-first search to return only one shortest path.

Phase 3: For each violated edge, we add the corresponding multicut constraints (8c) (possibly many) to our MILP (8)-(8e), where the left hand side corresponds to the paths found in phase 2.

Facet-defining searching strategy. The above mentioned strategy that finds violated constraints does not guarantee facet-defining inequalities. Recall that the multicut constraint (8c) is facet-defining if and only if the corresponding cycle is chordless. In the facet-defining searching strategy, we in addition keep track of the non-parental ancestors set (denoted S) of the current node during search. When we search for the next node, we make sure that the potential node does not form an edge (with respect to G) with any node in S .

5 Computational Experiments

In this section, all the experiments are conducted on a desktop with Intel(R) Xeon(R) CPU E5-2620 v4 @ 2.10GHz CPU and 64 GB memory, using IBM ILOG Cplex V12.8.0 as the MIP optimization solver.

We develop and compare the following variants of (8)-(8e) and report their computational results. The experiments are based on synthetic images of different sizes, as well as real depth images. We normalize the intensity values of all images to $[0, 1]$, and each experiment is conducted 3 times and only the median of the results is reported. We report the running time, nodes of the branch and bound tree, optimality gap, cuts added and the objective function of the MILP.

- **MP:** The MILP formulation of the piecewise affine fitting model (8)-(8e) that adds the multicuts without the facet-defining searching strategy.

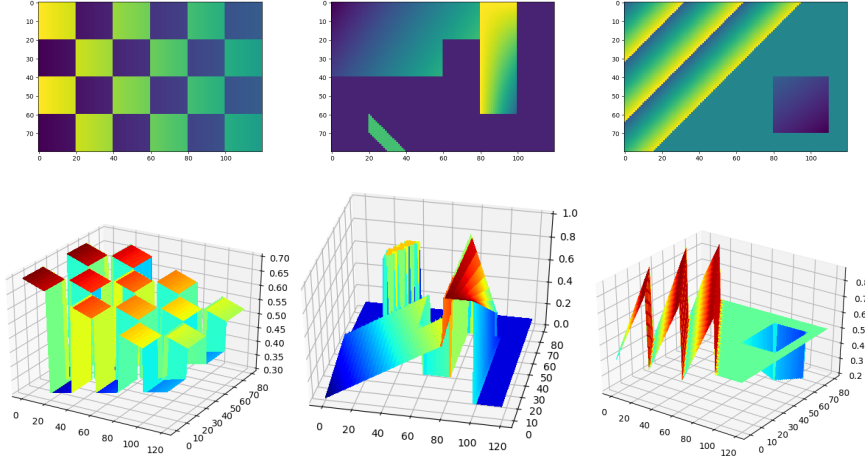


Fig. 7: Top: synthetic images with affine pieces, 2D view. Bottom: Their 3D views.

- **MPH**: MP where we adopt the solution of our heuristic as an initial input.
- **MPH-4**: MPH with the 4-edge cycle multicut constraints as initial inequalities.
- **MPH-4&8**: MPH with the 4 and 8-edge cycle multicut constraints.
- **MPH-F**: MPH with the facet-defining searching strategy.

5.1 Automatic computation of parameters

Parameter λ is the regularization term employed to avoid over-fitting in problem MP (8)-(8e). We set λ independently for each row and column, denoted λ_i^r and λ_j^c , since intuitively, this may help adapt to local features. λ is computed in a way to avoid making an outlier a one-node segment. Let $\lambda_i^r = \frac{1}{2}\xi \cdot \max_i |\nabla^2 y_i^r|$ and $\lambda_j^c = \frac{1}{2}\xi \cdot \max_j |\nabla^2 y_j^c|$, where ξ is the user-defined parameter. In this manner, if there exists an outlier (i, j) , making a one-node segment will active all four edges of (i, j) , thus incurring a penalty value of $2(\lambda_i^r + \lambda_j^c)$.

Parameter M is for the “big M” constraint in MP (8)-(8e). In principle, it should be big enough so that the constraints (8a,8b) are always valid, i.e., $M = 2$. On the other hand, it should be not too big, or it may harm the tightness of the LP relaxation. The value of big M could be computed automatically each on row and column, following the strategy above. However, we have tested different variants and found out the results only have slight fluctuations. Hence, we simply set $M = 2$ globally.

5.2 Detailed comparison on synthetic images

In this section, we generate 3 synthetic images that has affine trends, as shown in Figure 7. We then test different variants of our models on 3 sizes of the images, i.e.,

Size	Noises	Image	Test	MP(without heuristic)					MPH (with heuristic)					MPH-F(Add facet-defining cut)						
				Time	Nodes	Gap	Cuts	Obj	Time	Nodes	Gap	Cuts	Obj	Time	Nodes	Gap	Cuts	Obj		
20 × 30	0		1	1	0.13	0	0.00%	0	15.08	0.15	0	0.00%	0	15.08	0.15	0	0.00%	0	15.08	
			2	2	1.52	0	0.00%	1387	14.23	0.58	0	0.00%	316	14.23	0.56	0	0.00%	67	14.23	
			3	3	1.27	0	0.00%	1179	12.89	1.09	0	0.00%	69	12.89	1.70	0	0.00%	16	12.89	
	0.001		1	4	16.08	47636	0.00%	1345	15.50	96.18	730642	0.00%	2041	15.50	78.21	798080	0.00%	459	15.50	
			2	5	92.21	360426	0.00%	1244	14.81	169.28	1239650	0.00%	156	14.81	49.81	275858	0.00%	36	14.81	
			3	6	17.24	27351	0.00%	1110	13.36	54.65	163552	0.00%	7076	13.36	34.52	209820	0.00%	363	13.36	
		0.005	1	7	600.00	1616377	1.45%	2404	17.22	600.00	1899973	2.36%	1343	17.22	600.00	3659556	2.16%	207	17.22	
			2	8	600.00	656369	4.69%	1564	17.15	600.00	2152294	4.85%	208	17.15	600.00	2539081	4.92%	28	17.15	
			3	9	600.00	871831	1.81%	1911	15.24	600.00	1687239	3.03%	1420	15.24	600.00	1793897	2.83%	1389	15.24	
	40 × 60	0		1	10	0.37	0	0.00%	0	29.83	0.51	0	0.00%	0	29.83	0.52	0	0.00%	0	29.83
				2	11	2.56	0	0.00%	149	27.31	1.04	0	0.00%	187	27.31	1.09	0	0.00%	43	27.31
				3	12	7.76	0	0.00%	2172	26.35	25.45	3132	0.00%	2458	26.35	16.07	2958	0.00%	320	26.35
0.001			1	13	600.00	701107	1.71%	1030	31.90	600.00	1356351	1.80%	860	31.76	600.00	1436192	1.79%	160	31.76	
			2	14	600.00	45067	93.92%	25341	473.35	600.00	75493	85.45%	78491	195.39	600.00	172894	85.44%	46377	195.39	
			3	15	600.00	36378	92.33%	39972	362.24	600.00	100864	9.17%	59165	30.14	600.00	151291	3.04%	11846	28.30	
		0.005	1	16	600.00	145541	3.90%	5152	39.60	600.00	807142	7.39%	1411	39.74	600.00	860402	7.06%	279	39.60	
			2	17	600.00	14341	95.23%	13711	747.86	600.00	74864	88.61%	61615	299.80	600.00	139636	15.33%	24736	40.46	
			3	18	600.00	11414	93.29%	14163	513.11	600.00	37777	9.44%	62233	36.93	600.00	103259	8.17%	38910	36.43	
80 × 120		0		1	19	1.43	0	0.00%	0	59.32	1.93	0	0.00%	0	59.32	1.95	0	0.00%	0	59.32
				2	20	5.69	0	0.00%	249	53.60	5.14	0	0.00%	249	53.60	5.78	0	0.00%	70	53.60
				3	21	114.26	2096	0.00%	7263	52.50	71.99	3257	0.00%	5770	52.50	78.24	4039	0.00%	2721	52.50
	0.001		1	22	600.00	21367	95.58%	21044	1478.01	600.00	51544	66.33%	12051	191.29	600.00	192253	66.33%	1674	191.29	
			2	23	600.00	28275	97.97%	5029	2958.57	600.00	201047	93.36%	0	876.07	600.00	222030	93.36%	0	876.07	
			3	24	600.00	30419	97.13%	4952	2047.59	600.00	190999	92.08%	0	710.26	600.00	204646	92.08%	0	710.26	
		0.005	1	25	600.00	3	93.80%	5488	1505.13	600.00	100800	88.51%	150957	778.97	600.00	99766	88.51%	7476	778.97	
			2	26	600.00	0	100.00%	5610	-	600.00	61395	94.27%	0	1486.56	600.00	59694	94.27%	0	1486.56	
			3	27	600.00	0	100.00%	5802	-	600.00	43963	92.15%	139344	1066.30	600.00	47639	92.15%	65808	1066.30	

Fig. 8: Table on MP, MPH and MPH-F.

20 × 30, 40 × 60, and 80 × 120. In addition, we further experiments on scenarios that add Gaussian noise of level 0, 0.001 and 0.005. Thus, a total of 27 tests (81 experiments, as we run each test 3 times and only report the medium) are done for each model. We set the time limit of each experiment to 600 seconds.

Before starting these 81 experiment, we run additional experiments to select the “right” values of ξ . Since all three images already output optimal segmentation (with respect to the ground truth) results when $\xi = 0.5$, we keep it fixed throughout this section to keep our comparison concise.

5.2.1 MP vs MPH

We first conduct experiments on solving MP with and without the heuristic algorithms (introduced in Section 4.1) to the MIP solver. Our heuristic algorithm is fast to compute, takes 3 seconds on average to converge on the 40 × 60 sized images. Note that we only provide the MIP solver with initial integer solutions x of problem (8)-(8e), hence it takes time for the solver to compute w by solving a linear program.

As we can see in the MP column of Figure 8, MIP alone suffices to find optimal solutions in all tests when the image is clean (without Gaussian noise), even in 80 × 120 size. It also reaches optimality on the 20 × 30 images, with 0.001 Gaussian noise added. However, without heuristic, no feasible solution are found in Test 26 and 27 within 600 seconds. The results in MPH column indicates that adding the result of the heuristic as initial solution to the MIP solver mostly improves the results. For instance, MPH helps reduce the optimality gap from 92.33% to 9.17% in Test 15. It sometimes also reduce the performance, i.e., increases the running time of finding optimal solution from 16.08 to 96.18 seconds in Test 4.

Size	Noises	Image	Test	MPH (with heuristic)					MPH-4 (with 4cycle constraints)					MPH-4&8 (with 4cycle+8cycle constraints)						
				Time	Nodes	Gap	Cuts	Obj	Time	Nodes	Gap	Cuts	Obj	Time	Nodes	Gap	Cuts	Obj		
20 * 30	0		1	1	0.15	0	0.00%	0	15.08	0.20	0	0.00%	0	15.08	0.68	0	0.00%	0	15.08	
			2	2	0.58	0	0.00%	316	14.23	0.19	0	0.00%	0	14.23	0.31	0	0.00%	0	14.23	
			3	3	1.09	0	0.00%	69	12.89	0.16	0	0.00%	0	12.89	0.29	0	0.00%	0	12.89	
			4	4	96.18	730642	0.00%	2041	15.50	20.98	950	0.00%	0	15.50	28.89	1267	0.00%	0	15.50	
			5	5	169.28	1239650	0.00%	156	14.81	25.68	5809	0.00%	0	14.81	42.76	3667	0.00%	0	14.81	
			6	6	54.65	163552	0.00%	7076	13.36	13.36	5302	0.00%	0	13.36	29.21	4913	0.00%	0	13.36	
	0.001			1	7	600.00	1869973	2.36%	1343	17.22	600.00	569406	1.05%	0	17.22	600.00	250290	1.74%	0	17.22
				2	8	600.00	2152294	4.85%	208	17.15	600.00	446507	4.41%	0	17.15	600.00	259617	4.98%	0	17.15
				3	9	600.00	1687239	3.03%	1420	15.24	403.63	616255	0.00%	0	15.24	600.00	298515	0.88%	0	15.24
				1	10	0.51	0	0.00%	0	29.83	0.65	0	0.00%	0	29.83	1.59	0	0.00%	0	29.83
				2	11	1.04	0	0.00%	187	27.31	0.98	0	0.00%	0	27.31	1.63	0	0.00%	0	27.31
				3	12	25.45	3132	0.00%	2458	26.35	0.53	0	0.00%	0	26.35	1.31	0	0.00%	0	26.35
40 * 60	0		1	13	600.00	1356351	1.80%	860	31.76	600.00	102811	1.71%	0	31.76	600.00	24212	2.14%	0	31.76	
			2	14	600.00	75493	85.45%	78491	195.38	600.00	106217	3.89%	110	29.79	600.00	47433	4.00%	1	29.79	
			3	15	600.00	100984	9.17%	59165	30.14	600.00	62284	2.44%	0	28.30	600.00	26151	2.74%	0	28.30	
			1	16	600.00	807142	7.39%	1411	39.74	600.00	20627	6.94%	0	39.60	600.00	3843	7.02%	0	39.60	
			2	17	600.00	74864	88.61%	61615	299.80	600.00	24661	13.65%	0	39.69	600.00	1897	13.55%	0	39.69	
			3	18	600.00	37777	9.44%	62233	36.93	600.00	18969	8.98%	0	36.96	600.00	3899	6.69%	0	36.10	
	0.001			1	19	1.93	0	0.00%	0	59.32	2.29	0	0.00%	0	59.33	3.85	0	0.00%	0	59.33
				2	20	5.14	0	0.00%	249	53.60	4.63	0	0.00%	0	53.60	6.82	0	0.00%	0	53.60
				3	21	71.99	3257	0.00%	5770	52.50	2.50	0	0.00%	0	52.50	4.81	0	0.00%	0	52.50
				1	22	600.00	51544	66.33%	12051	191.29	600.00	258	3.84%	0	67.14	600.00	0	82.19%	0	191.29
				2	23	600.00	201047	93.36%	0	876.07	600.00	2983	93.34%	0	876.07	600.00	233	93.34%	0	876.07
				3	24	600.00	190999	92.08%	0	710.26	600.00	8388	92.04%	0	710.26	600.00	0	92.06%	0	710.26
80 * 120	0		1	25	600.00	100800	88.51%	150957	776.87	600.00	0	93.94%	0	776.87	600.00	0	93.94%	0	776.87	
			2	26	600.00	61395	94.27%	0	1486.56	600.00	0	95.65%	0	1486.56	600.00	0	95.65%	0	1486.56	
			3	27	600.00	43963	92.15%	139344	1066.30	600.00	0	94.19%	0	1066.30	600.00	0	94.19%	0	1066.30	
			1	28	600.00	100800	88.51%	150957	776.87	600.00	0	93.94%	0	776.87	600.00	0	93.94%	0	776.87	
			2	29	600.00	61395	94.27%	0	1486.56	600.00	0	95.65%	0	1486.56	600.00	0	95.65%	0	1486.56	
			3	30	600.00	43963	92.15%	139344	1066.30	600.00	0	94.19%	0	1066.30	600.00	0	94.19%	0	1066.30	

Fig. 9: Table on MPH, MPH-4 and MPH-4&8.

5.2.2 MPH vs MPH-F

Given an heuristic solution, we further test the performance of adopting the facet-defining searching strategy. Recall that although it takes more time to find a facet-defining multicut constraint (8c) (as described in the facet-defining searching strategy), it is tighter compared to non facet-defining ones. The results are shown in the MPH and MPH-F columns of Figure 8, where we could see MPH-F performs better than MPH in most of the cases, with only a few exceptions. For instance, MPH-F helps reduce the running time from 169.28 to 149.81 seconds in Test 5. MPH-F also reduces the optimality gap from 88.61% to 15.33% in Test 17.

5.2.3 MPH vs MPH-4 and MPH-4&8

We compare whether adding few facet-defining multicut constraints as initial constraints to MPH improves computation. We test the performance of adding only 4-cycle constraints (MPH-4) and adding both 4-cycle and 8-cycle (MPH-4&8). The results are shown in Figure 9. We notice that after adding these cycle constraints, Cplex rarely add any additional cuts to MPH. We also note that in general, adding 4-cycle constraints helps on improving the performance. For instance, MPH-4 reduces the optimality gap significantly on test 14, test 17 and test 22. In addition, compared to MPH-4, the experiments shows that adding the 8-cycle constraints seems harmful in most cases.

5.2.4 Results on segmentation and denoising

Upon solving our MILP (8)-(8e), the active edges ($x_e = 1$) together with the multicut constraints (8c) form a valid segmentation, and the fitting variables (w) removes noise. Although only an approximate formulation, the segmentation results of most tests (except for Test 25-27) already achieve “optimal” compared to the ground truth.

An illustration of the denoising results (as well as segmentation) can be seen in Figure 10, where the first row are the 40×60 images with 0.005 Gaussian noise, and second row the results from MPH-4.

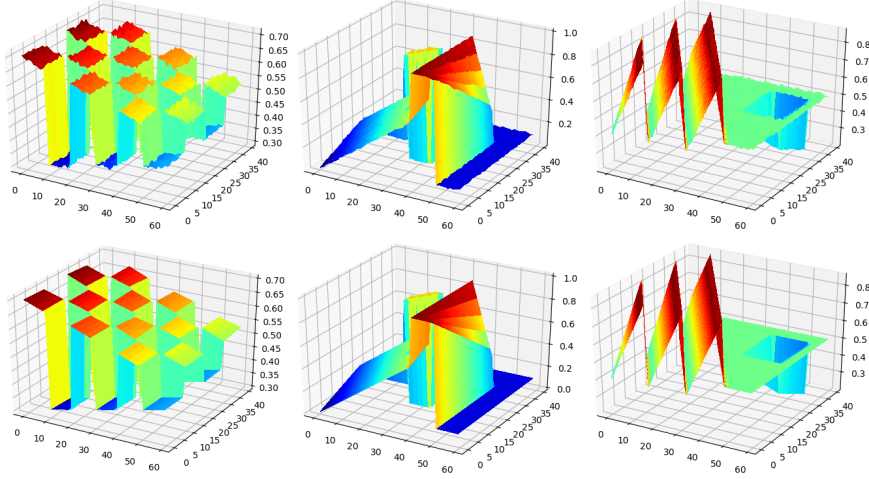


Fig. 10: Top: images (40×60) with Gaussian noise. Bottom: results from MPH-4.

5.3 Detailed comparison on real images

We further conduct experiments on two real depth images with 2 different sizes (600 pixels and 2400 pixels), which are generated from the disparity maps of the Middlebury data set [18] (shown in Figure 11).

According to the performance of the models in previous section, we choose to test different variants (with respect to ξ and time limit) of MPH-4-F (MPH with the 4-edge cycle multicut constraints using the facet-defining searching strategy). Since real images already contain noise, we do not add extra noise. We also run each experiment 3 times and only report the medium. All the results are shown in Figure 12.

5.3.1 Regularization parameter ξ

The regularization parameter ξ is introduced to penalize the perimeter as well as the number of segments. The larger ξ is, the fewer the segments are. In this section, we conduct experiments on using 3 different value of parameter ξ (0.5, 1 and 2), and the time limit is set to 1200 seconds.

The computational results are shown in the left table of Figure 12. However, since the objective functions contain both fitting and regularization terms, their absolute values is not comparable. Instead, we visualize the segmentation results in Figure 13. It is obvious to see that the number of segments decreases as ξ increases.

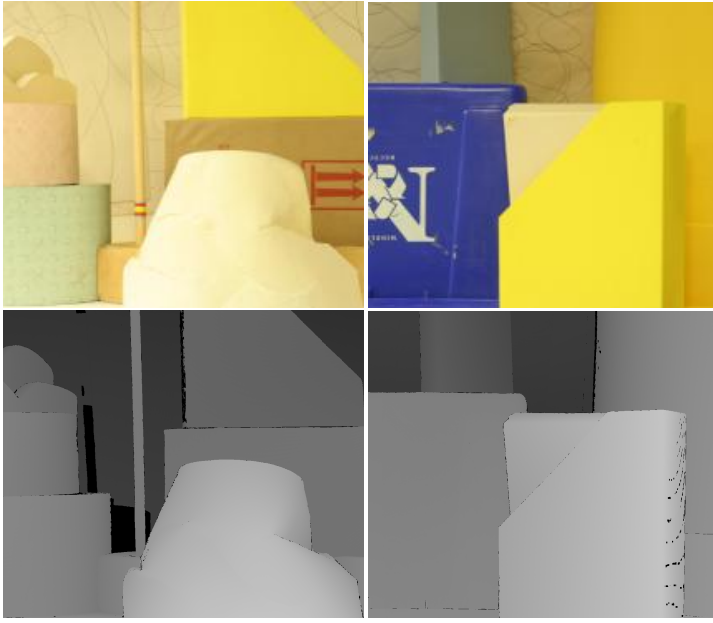


Fig. 11: Top: Two images from [18]. Bottom: their disparity maps.

Regularization	Size	Image	Nodes	Gap	Cuts	Obj
0.5	600	1	1130786	13.26%	73	23.83
		2	953449	20.87%	62	10.33
	2400	1	199981	31.36%	1304	55.80
		2	207515	68.53%	923	49.22
1	600	1	388654	29.22%	23	39.23
		2	704727	26.85%	0	17.25
	2400	1	97947	58.15%	230	128.26
		2	77947	71.07%	89	78.68
2	600	1	175870	50.62%	0	64.85
		2	330469	39.15%	0	30.12
	2400	1	15997	65.77%	23	204.76
		2	21161	73.14%	8	126.23

Time Limit	Size	Image	Nodes	Gap	Cuts	Obj
50	600	1	42419	18.37%	50	24.66
		2	32686	29.68%	24	11.04
	2400	1	3542	67.59%	3	115.47
		2	5645	74.02%	23	56.63
200	600	1	174667	15.62%	76	24.09
		2	144267	25.76%	27	10.59
	2400	1	48493	67.01%	317	113.49
		2	73578	72.60%	78	53.63
600	600	1	517647	13.60%	110	23.58
		2	407278	23.26%	31	10.46
	2400	1	152334	40.13%	748	62.75
		2	197158	70.52%	886	50.22
1200	600	1	1130786	13.26%	73	23.83
		2	953449	20.87%	62	10.33
	2400	1	199981	31.36%	1304	55.80
		2	207515	68.53%	923	49.22

Fig. 12: Table of tests on MPH-4-F with different regularization parameters ξ and time limits.

5.3.2 Time limit

In this section, we conduct experiments on adopting 4 time limits (50, 200, 600 and 1200 seconds), and we set $\xi = 0.5$. The computational results are shown in the right table of Figure 12. Since none of tests finds the optimal, the performance could possibly be further improved by extending the time limit. In addition, a shorter time limit is still possible to produce a solution with acceptable gap, especially for images with smaller size. Figure 14 visualizes the optimality gap with respect to time limit. As can be predicted, when time limit increases, the optimality gap drops.

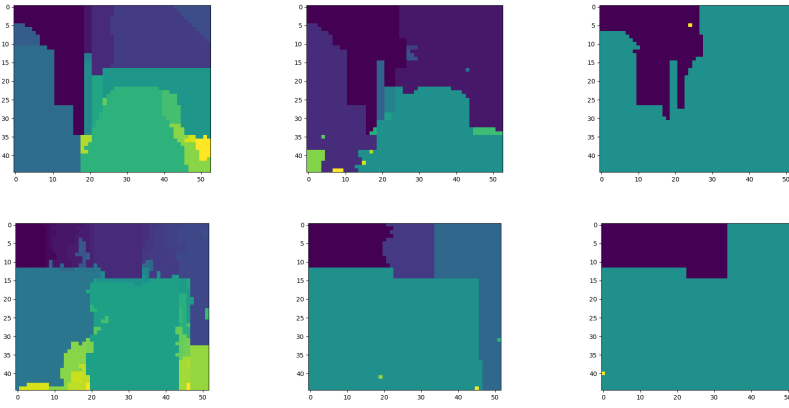


Fig. 13: Segmentation results as the ξ increases from left to right.

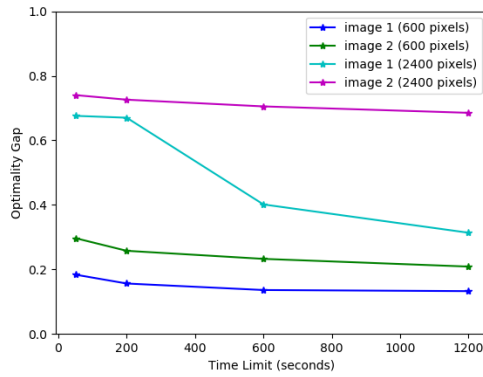


Fig. 14: Optimality gap decreases as time limit increases.

6 Conclusions

In this paper, we have presented a unsupervised and non-parametric model that approximates a discontinuous piecewise affine function to fit the given data. We formulate it as a MIP and solve it with a standard optimization solver. Although not an exact model in 2D, the inclusion of multicut constraints enables a feasible segmentation of the image domain. Thus, a corresponding piecewise affine function can be easily reconstructed.

The computational complexity is the main bottleneck of our approach. To tackle with it, we add two different sets of facet-defining inequalities to our MIP. We also implemented a special heuristic algorithm that finds a feasible segmentation, which is used as an initial integer solution to the MIP solver. We conducted extensive experiments on different variants of our model and study the effects of adjusting model

parameters. We demonstrate the feasibility of our approach by its applications to segmentation and denoising on both synthetic and real depth images.

As for future work, the 8-neighbor relations of the square grid graph in 2D is worth investigating, as well as its generalization to 3D images. Furthermore, we will extend this work beyond the scope of image segmentation and denoising to deal with other applications, such as signal compression[3] and optical flow [6].

References

1. Amaldi, E., Coniglio, S., Taccari, L.: Discrete optimization methods to fit piecewise affine models to data points. *Computers and Operations Research* pp. 214–230 (2016). <https://doi.org/10.1016/j.cor.2016.05.001>
2. Andres, B., Kappes, J.H., Beier, T., Köthe, U., Hamprecht, F.A.: Probabilistic image segmentation with closedness constraints. pp. 2611–2618 (2011)
3. Duarte, M.F., Shen, G., Ortega, A., Baraniuk, R.G.: Signal compression in wireless sensor networks. *Philosophical transactions. Series A, Mathematical, physical, and engineering sciences* **370** **1958**, 118–35 (2012)
4. Ferrari-Trecate, G., Muselli, M.: A new learning method for piecewise linear regression. In: ICANN (2002)
5. Ferrari-Trecate, G., Muselli, M., Liberati, D., Morari, M.: A clustering technique for the identification of piecewise affine systems. In: Di Benedetto, M.D., Sangiovanni-Vincentelli, A. (eds.) *Hybrid Systems: Computation and Control*. pp. 218–231. Springer Berlin Heidelberg, Berlin, Heidelberg (2001)
6. Fortun, D., Storath, M., Rickert, D., Weinmann, A., Unser, M.: Fast piecewise-affine motion estimation without segmentation. *IEEE Transactions on Image Processing* **27**(11), 5612–5624 (Nov 2018). <https://doi.org/10.1109/TIP.2018.2856399>
7. Geman, S., German, D.: Stochastic relaxation, gibbs distributions, and the bayesian restoration of images. *IEEE Transactions on Pattern Analysis and Machine Intelligence* **6**, 721–741 (1984). <https://doi.org/10.1109/TPAMI.1984.4767596>
8. Hayder, Z., He, X., Salzmann, M.: Boundary-aware instance segmentation. 2017 IEEE Conference on Computer Vision and Pattern Recognition (CVPR) pp. 587–595 (2016)
9. Horňáková, A., Lange, J., Andres, B.: Analysis and optimization of graph decompositions by lifted multicuts. In: *Proceedings of the 34th International Conference on Machine Learning*. vol. 70, pp. 1539–1548 (2017)
10. Kappes, J.H., Speth, M., Andres, B., Reinelt, G., Schnörr, C.: Globally optimal image partitioning by multicuts. In: *Proceedings of the International Workshop on Energy Minimization Methods in Computer Vision and Pattern Recognition*. pp. 31–44 (2011), 1
11. Kappes, J., Speth, M., Reinelt, G., Schnörr, C.: Towards efficient and exact map-inference for large scale discrete computer vision problems via combinatorial optimization. In: *Proceedings of the IEEE Conference on Computer Vision and Pattern Recognition (CVPR)*. pp. 1752–1758 (2013). <https://doi.org/10.1109/CVPR.2013.229>
12. Kappes, J., Speth, M., Reinelt, G., Schnörr, C.: Higher-order segmentation via multicuts. *Computer Vision and Image Understanding* **143**, 104 – 119 (2016). <https://doi.org/https://doi.org/10.1016/j.cviu.2015.11.005>, <http://www.sciencedirect.com/science/article/pii/S1077314215002490>, inference and Learning of Graphical Models Theory and Applications in Computer Vision and Image Analysis
13. LeCun, Y., Bengio, Y., Hinton, G.: Deep learning. *Nature* **521**(7553), 436–444 (5 2015). <https://doi.org/10.1038/nature14539>
14. Lysaker, M., Tai, X.: Iterative image restoration combining total variation minimization and a second-order functional. *International Journal of Computer Vision* **66**(1), 5–18 (2006). <https://doi.org/10.1007/s11263-005-3219-7>, <https://doi.org/10.1007/s11263-005-3219-7>
15. Nguyen, R.M.H., Brown, M.S.: Fast and effective l0 gradient minimization by region fusion. In: *Proceedings of the IEEE International Conference on Computer Vision (ICCV)*. pp. 208–216 (2015)
16. Potts, R.B., Domb, C.: Some generalized order-disorder transformations. *Proceedings of the Cambridge Philosophical Society* **48**, 106–109 (1952). <https://doi.org/10.1017/S0305004100027419>

17. Rudin, L., Osher, S., Fatemi, E.: Nonlinear total variation based noise removal algorithms. *Physica D* **60**, 259–268 (1992)
18. Scharstein, D., Pal, C.: Learning conditional random fields for stereo. In: 2007 IEEE Conference on Computer Vision and Pattern Recognition. pp. 1–8 (June 2007). <https://doi.org/10.1109/CVPR.2007.383191>
19. Seal, H.L.: Studies in the history of probability and statistics. xv: The historical development of the gauss linear model. *Biometrika* **54**(1-2), 1–24 (1967). <https://doi.org/10.1093/biomet/54.1-2.1>
20. Shelhamer, E., Long, J., Darrell, T.: Fully convolutional networks for semantic segmentation. *IEEE Transactions on Pattern Analysis and Machine Intelligence* **39**(4), 640–651 (April 2017). <https://doi.org/10.1109/TPAMI.2016.2572683>
21. Shen, R., Chen, X., Zheng, X., Reinelt, G.: Discrete Potts Model for Generating Superpixels on Noisy Images. arXiv e-prints arXiv:1803.07351 (Mar 2018)
22. Szeliski, R., Zabih, R., Scharstein, D., Veksler, O., Kolmogorov, V., Agarwala, A., Tappen, M., Rother, C.: A comparative study of energy minimization methods for markov random fields with smoothness-based priors. *IEEE Transactions on Pattern Analysis and Machine Intelligence* **30**(6), 1286–80 (2008). <https://doi.org/10.1109/TPAMI.2007.70844>
23. Toriello, A., Vielma, J.: Fitting piecewise linear continuous functions. *European Journal of Operational Research* **219**, 86–95 (2012)
24. Yang, X., Yang, H., Zhang, F., Zhang, L., Fan, X., Ye, Q., Fu, L.: Piecewise linear regression based on plane clustering. *IEEE Access* **7**, 29845–29855 (2019). <https://doi.org/10.1109/ACCESS.2019.2902620>